ADVANCED SCIENCE NEWS
www.advancedsciencenews.com

ADVANCED FUNCTIONAL MATERIALS
www.afm-journal.de

In Situ Reversible Ionic Control for Nonvolatile Magnetic Phases in a Donor/Acceptor Metal-Organic Framework

Kouji Taniguchi, Keisuke Narushima, Hajime Sagayama, Wataru Kosaka, Nanami Shito, and Hitoshi Miyasaka**

Reversible magnetic control by electrical means, which is highly desired from the viewpoint of fundamentals and technological applications such as data storage devices, has been a challenging topic. In this study, the authors demonstrate in situ magnetic phase switching between the ferrimagnetic and paramagnetic states of an electron-donor/-acceptor metal-organic framework (D/A-MOF) using band-filling control mediated by the Li$^+$-ion migration that accompanies redox reactions, i.e., "magneto-ionic control". By taking advantage of the rechargeability of lithium-ion battery systems, in which Li$^+$-ions and electrons are simultaneously inserted into/extracted from a cathode material, the reversible control of nonvolatile magnetic phases in a D/A-MOF has been achieved. This result demonstrates that the combination of a redox-active MOF with porous flexibility and ion-migration capability enables the creation of new pathways toward magneto-electric coupling devices in the field of ionics.

1. Introduction

The reversible electrical control of magnetism[1–3] has become one of the central issues in the fields of spintronics and materials science.[4–6] One effective approach for achieving the reversible electrical control of magnetism is to modulate the electron density in correlated electron systems, i.e., band-filling control. A class of thin films made from diluted magnetic semiconductors and magnetic metals has been used to successfully demonstrate electrostatic band-filling control of magnetism through the application of the field-effect transistor principle;[7–13] however, direct detection of the modulated magnetization has, to date, been difficult because the applied electric fields were limited to a thickness of one nanometer or less as the result of the presence of the electrostatic screening effect. Consequently, the induced magnetic moments were manipulated only in small thin interfacial areas. Thus, further development of band-filling control methods, which can also be applied for bulk materials, is highly desirable for the development of advanced devices in which intrinsic magnetic moments are critical for functionality.

Another approach for the electrical control of magnetism is to use ion-migration associated with redox reactions, which has recently been termed "magneto-ionic control".[14–20] Broadly speaking, this technique has attracted much attention in a wide variety of systems, not only for heterointerfaces between metals and oxides[14–19] or thin film compounds,[21,22] but also for bulk magnetic control in transition-metal oxides,[23–26] octacyanometallate-bridged coordination polymers,[27] Prussian blue analogues[28–34] and donor/acceptor metal-organic frameworks (D/A-MOFs).[35] Several reports have been based on the migration of oxygen anions (O^{2-}) preorganized in materials,[14–20] but it is also possible to induce a drastic change in the magnetic properties of a material using ion-insertion based on a postsynthetic method; this is an electrochemical doping method associated with the simultaneous introduction/extraction of electrons and ions to targets,[27,28,31,35] which consequently enables the creation of an artificial material that can be switched using an ion-insertion device.

Lithium-ion batteries (LIBs) are well-known energy storage systems in our society;[36] they are representative ion-insertion devices. In LIBs, Li$^+$-ions and electrons are shuttled between the cathode and anode in a discharge/charge process (**Figure 1**a). In the discharge process, Li$^+$-ions are inserted into the void space of the cathode material and electrons are simultaneously doped into the cathode material, i.e., the material undergoes reduction to maintain an electrically neutral equilibrium. Importantly, Li$^+$-ions and electrons are likely

---

Dr. K. Taniguchi, Dr. W. Kosaka, Prof. H. Miyasaka
Institute for Materials Research (IMR)
Tohoku University
2-1-1 Katahira, Aoba-ku, Sendai 980-8577, Japan
E-mail: taniguchi@imr.tohoku.ac.jp;
miyasaka@imr.tohoku.ac.jp

Dr. K. Taniguchi, K. Narushima, Dr. W. Kosaka, N. Shito,
Prof. H. Miyasaka
Department of Chemistry
Graduate School of Science
Tohoku University
6-3 Aramaki-Aza-Aoba, Aoba-ku, Sendai 980–8578, Japan

Dr. K. Taniguchi
Elements Strategy Initiative for Catalysts and Batteries (ESICB)
Kyoto University
Nishikyo-ku, Kyoto 615-8510, Japan

Dr. H. Sagayama
Institute of Materials Structure Science
High Energy Accelerator Research Organization
Tsukuba, Ibaraki 305-0801, Japan

DOI: 10.1002/adfm.201604990

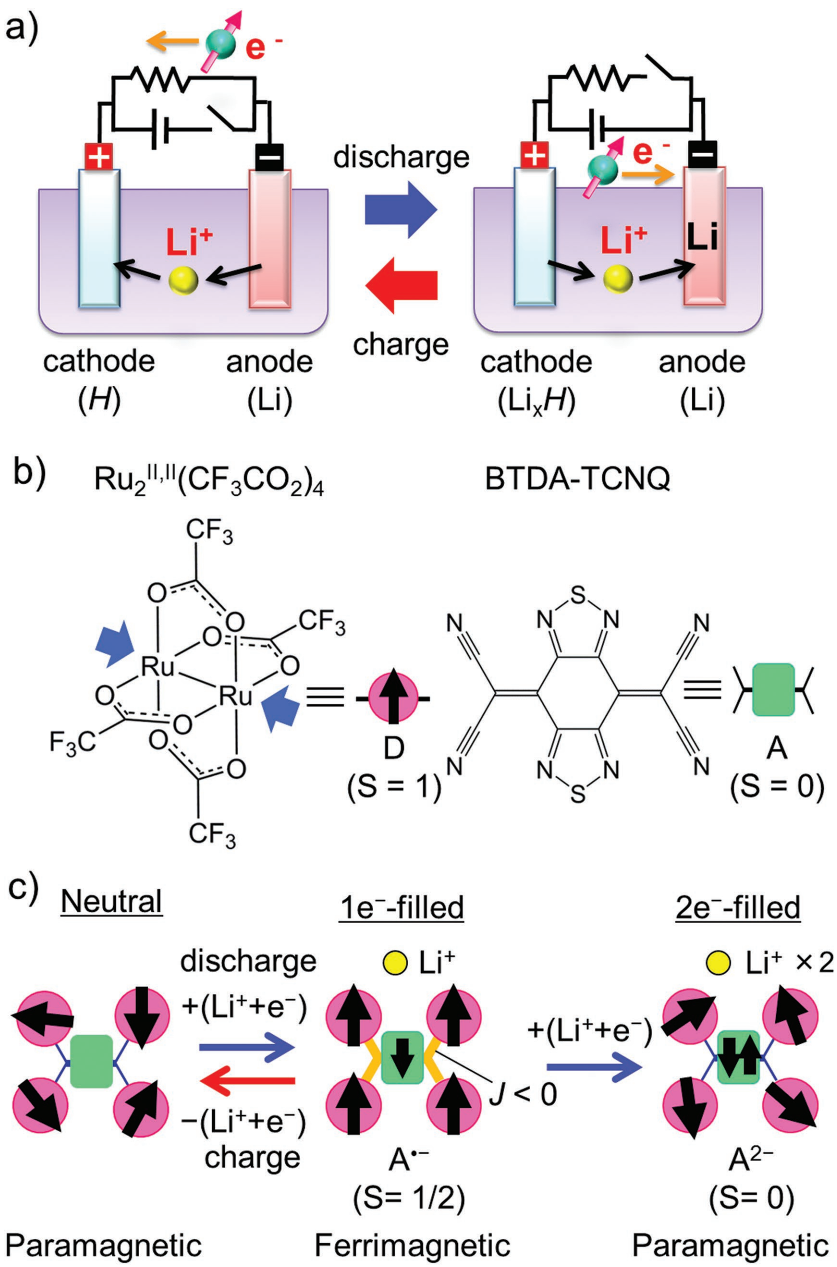

Figure 1. Magnetism control using a Li$^+$-ion battery system. a) Schematic illustration of a LIB. In the discharge process, Li$^+$-ions and electrons are simultaneously introduced into a host material (*H*) in the cathode. In the charge process, the inserted Li$^+$-ions and electrons are extracted from the cathode. b) Schematic representation of $[Ru_2^{II,II}(CF_3CO_2)_4]$ ($[Ru_2^{II,II}]$) ($S = 1$) as the electron donor (D) and BTDA-TCNQ ($S = 0$) as the electron acceptor (A). Blue arrows represent the axial sites of $[Ru_2^{II,II}(CF_3CO_2)_4]$, to which four CN groups of BTDA-TCNQ coordinate to form a D_2A network. c) Conceptual Figure of magnetic phase switching between paramagnetic and ferrimagnetic states mediated by an LIB system. One-electron-filling of the A-site in a neutral D_2A compound induces an ionic ferrimagnetic state (1e$^-$-filled state) through antiferromagnetic exchange interaction ($J < 0$). The electron extraction from the $A^{\bullet-}$ radical ($S = 1/2$) during the charge process of a LIB system restores a neutral paramagnetic state. On the other hand, two-electron-filling of the A-site destabilizes the ionic ferrimagnetic state and produces an ionic paramagnetic state (2e$^-$-filled state) because A^{2-} ($S = 0$) disconnects the exchange paths.

stabilized separately at different sites in a cathode material because a Li$^+$-ion has a much smaller ionization potential. On the other hand, the doped electrons can be removed during the charging process (i.e., the reduced cathode material is oxidized to the original neutral material) through Li$^+$-ion extraction (see Figure 1a). Thus, an LIB system can be regarded as a device that involves reversible band-filling at redox active electrode materials. Indeed, an LIB system has been used for the reversible control of magnetism in bulk materials.[24,25,33] Nevertheless, magneto-ionic control using LIB systems has so far been limited to varying the magnetic moments within a pre-existing magnetically ordered state. There has been no report detailing the use of LIBs in the development of a magnetic phase control.

Here, we demonstrate a reversible magnetic "phase switching" between disordered and ordered states in a D/A-MOF used as the cathode material of an LIB through discharge/charge cycles. The D/A-MOF used here has a D_2A formula that consists of carboxylate-bridged paddlewheel-type diruthenium(II,II) complexes ($[Ru_2^{II,II}]$) as the donor (D) units, and 7,7,8,8-tetracyano-*p*-quinodimethane (TCNQ) derivatives (TCNQ*R*) as the acceptor (A) units (Figure 1b).[37] This class of porous crystalline materials, which are expected to accommodate Li$^+$-ions flexibly, has been shown to exhibit solvation-associated crystal-to-crystal transformations.[38] It should be also emphasized here that long-range magnetic order in $[Ru_2]$/TCNQ*R*-MOF appears only when the $A^{\bullet-}$ radical (TCNQ$R^{\bullet-}$) is present.[37] The origin of long-range magnetic order is ascribed to an antiferromagnetic exchange interaction between the spin of $[Ru_2^{II,II}]^0$ with $S = 1$ (or $[Ru_2^{II,III}]^+$ with $S = 3/2$) and that of TCNQ$R^{\bullet-}$ with $S = 1/2$.[37,39] Focusing on this characteristic, we have recently found that a ferrimagnetic lattice $[-\{Ru_2^{II,II}\}-TCNQR^{\bullet-}-\{Ru_2^{II,II}\}-]_n n^-$ can be artificially constructed from the neutral paramagnetic state $[-\{Ru_2^{II,II}\}-TCNQR^0-\{Ru_2^{II,II}\}-]_n$ by the generation of $A^{\bullet-}$ through electron-doping via Li$^+$-ion insertion.[35] Thus, if Li$^+$-ions were reversibly inserted into/extracted from the D/A-MOF through an LIB discharge/charge cycle, magnetic phase switching could be expected between the neutral paramagnetic ($D^0{}_2A^0$) state and the ferrimagnetic state with one-electron filled A ($D^0{}_2A^{\bullet-}$) (see Figure 1c). Based on this concept, we have achieved in situ magneto-ionic phase control for a new neutral layered D/A-MOF, $[\{Ru_2^{II,II}(CF_3CO_2)_4\}_2$(BTDA-TCNQ)]·*p*-xylene (**1′**; $CF_3CO_2^-$ = trifluoroacetate; BTDA-TCNQ = bis(1,2,5-thiadiazolo)tetracyanoquinodimethane).

2. Results

2.1. Materials Preparation

For the electrical control of magnetism in LIB systems, a neutral layered D/A-MOF with a $[-\{Ru_2^{II,II}\}-TCNQR^0-\{Ru_2^{II,II}\}-]_n$ lattice was selected as the starting material for the cathode. As a first approximation for the design of neutral layered D/A-MOFs, we can roughly predict the charge distribution in the $[\{Ru_2\}_2TCNQR]$-MOF system from the energy difference between the highest occupied molecular orbital (HOMO) level of D and the lowest unoccupied molecular orbital (LUMO) level of A, i.e., $\Delta E_{\text{H-L}}(\text{DA}) \equiv E_{\text{LUMO}}(\text{A}) - E_{\text{HOMO}}(\text{D})$, where $\Delta E_{\text{H-L}}(\text{DA}) > 0$ for the neutral state and $\Delta E_{\text{H-L}}(\text{DA}) < 0$ for the ionic state.[37] In this work, a combination of $[Ru_2^{II,II}(CF_3CO_2)_4(THF)_2]$ with $E_{\text{HOMO}}(\text{D}) = -5.6183$ eV[40] and BTDA-TCNQ with $E_{\text{LUMO}}(\text{A}) = -4.7353$ eV[41] (Figure 1b) was chosen to give a positive $\Delta E_{\text{H-L}}(\text{DA})$ value for the neutral D_2A (0.883 eV). Indeed, this D/A combination resulted in a new neutral D_2A-type layered MOF, $[\{Ru_2(CF_3CO_2)_4\}_2(\text{BTDA-TCNQ})]\cdot n\text{CH}_2\text{Cl}_2\cdot(p\text{-xylene})$ (**1**). Compound **1**, solvated by CH_2Cl_2 and *p*-xylene molecules, easily releases only the CH_2Cl_2 molecules at room temperature to produce the CH_2Cl_2-free compound, $[\{Ru_2(CF_3CO_2)_4\}_2(\text{BTDA-TCNQ})]\cdot(p\text{-xylene})$ (**1′**), which is stable even under vacuum (Figure S1, Supporting Information). This compound was used as the cathode material for the subsequent LIB measurements.

2.2. Materials Characterization

Compound **1** crystallizes in the monoclinic space group *C*2/*m* with an inversion center located at the midpoint of the Ru—Ru bonds. Only one [Ru$_2$] unit, lying on a C_2 axis, and one BTDA-TCNQ molecule, lying on the C_2 axis and a mirror plane, were crystallographically characterized as the asymmetric unit ($Z = 2$) (Figure S2, Supporting Information). A typical 2D fishnet framework parallel to the (20–1) plane is formed by the coordination of the four C≡N groups of the BTDA-TCNQ unit to the two axial sites of the [Ru$_2$] units (i.e., a D_2A-type structure) (Figure S2b,c, Supporting Information).[42] One *p*-xylene molecule per unit is located between the D_2A-layers, forming a *π*-stacked motif with the BTDA-TCNQ moieties through a [···BTDA-TCNQ···(*p*-xylene)···BTDA-TCNQ···] column along the *c* axis (interlayer direction).

The oxidation state of the [Ru$_2$] and BTDA-TCNQ units was confirmed by comparing the bond lengths in the respective units with those in standard compounds. The Ru—O$_{\text{eq}}$ (O$_{\text{eq}}$ = carboxylate oxygen atom) bond lengths are sensitive to the oxidation state of [Ru$_2$] and generally lie in the range 2.07–2.09 Å for $[Ru_2^{II,II}]$ and 2.01–2.03 Å for $[Ru_2^{II,III}]^+$.[43] The average Ru—O$_{\text{eq}}$ length of **1** is 2.064 Å (Table S1, Supporting Information), indicating an oxidation state of $[Ru_2^{II,II}]$ (neutral state), which also agrees with the neutral state of the BTDA-TCNQ moiety (Table S2, Supporting Information). The charge distribution in **1** was also confirmed by its magnetic properties, in which paramagnetic behavior for isolated $S = 1$ spins from two $[Ru_2^{II,II}]$ units was observed over the whole temperature range of 1.8–300 K (Figure S3, Supporting Information).

Compound **1′**, which was used in the investigation of magnetism control, crystallizes in the triclinic space group *P*–1, where two [Ru$_2$] units and one BTDA-TCNQ unit with inversion centers were structurally characterized as the asymmetric unit ($Z = 1$) (**Figure 2**a). The typical fishnet framework, parallel to the (11–1) plane, was maintained even after removal of the CH_2Cl_2 molecules under vacuum (Figure 2b,c). This result indicates that the combination of $Ru_2(CF_3CO_2)_4$ and BTDA-TCNQ undergoes a solvation-related crystal-to-crystal transformation, as observed in other [Ru$_2$]/TCNQ*R* MOFs,[38,44] and that it has great potential to be a flexible layered MOF for guest molecules/ions. Compound **1′** contains one *p*-xylene molecule per asymmetric unit, which is located between layers forming the same *π*-stacked motif with BTDA-TCNQs as found in **1**. The volume of the void space in **1′** is 152.7 Å^3, corresponding to 10.4% of the cell volume (the total volume of void and CH_2Cl_2-occupied space in **1** is 977.3 Å^3, corresponding to 28.7% of the cell volume; see Experimental Section). The average Ru—O$_{\text{eq}}$ length in **1′** is 2.080 Å, indicating an oxidation state of $[Ru_2^{II,II}]$; this structural characteristic proves that the neutral state is preserved in **1′** even after the structural changes induced by the removal of CH_2Cl_2 from **1**. Indeed, the paramagnetic characteristics were preserved in **1′** (Figure S4, Supporting Information).

2.3. Ex Situ Characterization of Electron-Doped Neutral D/A-MOF

Electron-doping of **1′** was carried out through Li$^+$-ion insertion using an LIB system, in which Li metal was employed as the anode (we use the term LIB in this work, but it is a half-cell of LIB and lithium battery). The cathode was fabricated by mixing crystals of **1′** with conductive acetylene black and polytetrafluoroethylene as the binder. A coin-type cell was assembled with an ionic liquid as the electrolyte medium,[45] and the rechargeable performance as a secondary battery was confirmed for 20 cycles (Figure S5, Supporting Information). The electrochemical Li$^+$-ion insertion was performed using the galvanostatic intermittent titration technique (GITT),[46] for which a constant low-density current (1.54 mA g^{-1}) was applied for 1 h followed by an interval of 1 h to achieve the electrochemical equilibrium state of **1′**. **Figure 3** displays the open circuit voltages (OCVs) of an LIB incorporating **1′** as the cathode. In general, the OCV (V_{OC}) is given by the difference in the electrochemical potentials for electrons between the anode ($\bar{\mu}_e^a$) and the cathode ($\bar{\mu}_e^c$): $eV_{\text{OC}} = \bar{\mu}_e^a - \bar{\mu}_e^c$, where e is the magnitude of the electron charge[47] (Figure S6, Supporting Information). In Figure 3, the OCV curve as a function of the capacity, which is the electric charge per unit weight, shows a decrease with the increasing capacity. Taking into account the fact that the electrochemical potential of an electron ($\bar{\mu}_e$) corresponds to the Fermi level of the electrode in an electrolyte, which is given by the chemical potential of the electron (μ_e) and the inner potential (ϕ): $\bar{\mu}_e = \mu_e - e\varphi$,[48] the OCV profile reflects the variation of the Fermi level of the electrode. In the case of an Li metal anode, the Fermi level of Li remains unchanged during the discharge process; hence, the decrease in the OCV observed in Figure 3

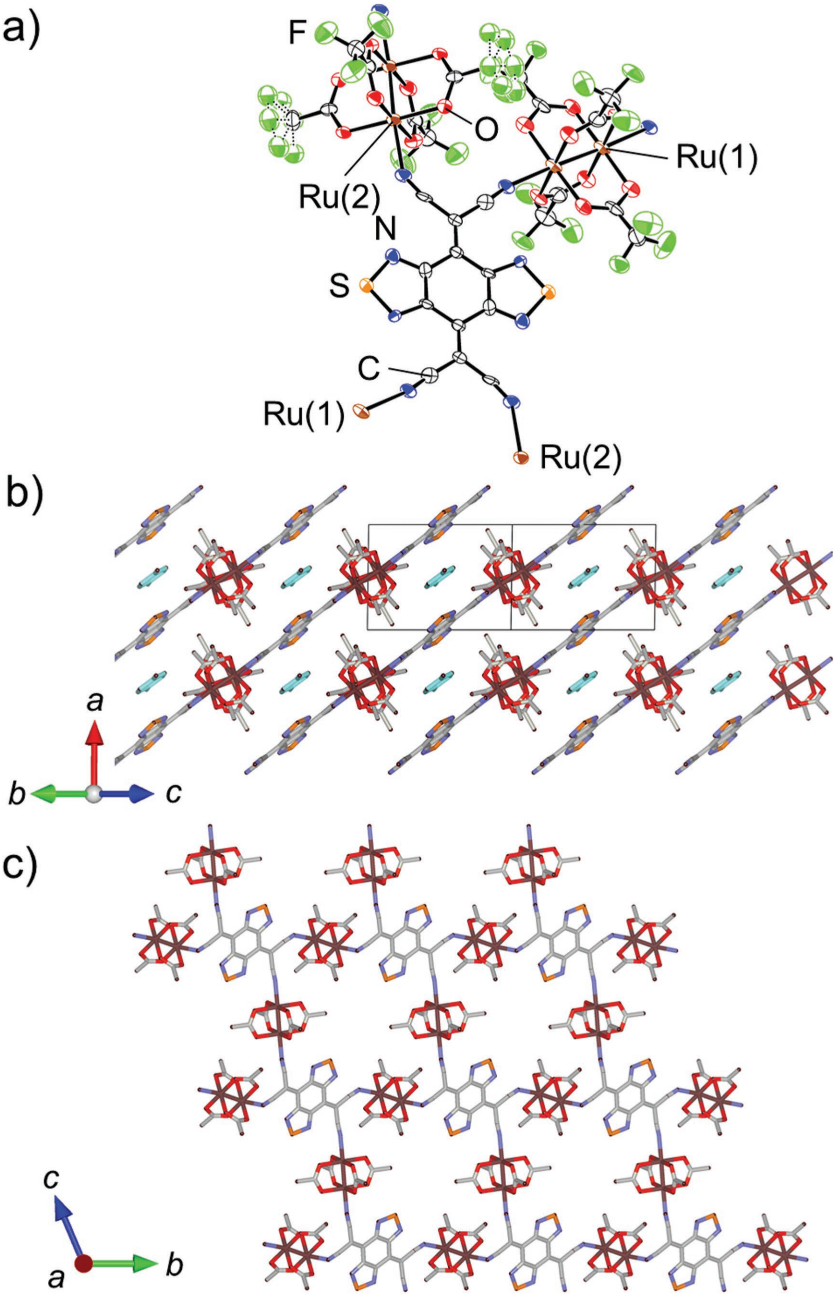

Figure 2. Crystal structure of **1′**. a) Thermal ellipsoid plots of the formula unit of **1′**, where C–F bonds with disordered F-atoms are represented by dotted lines (solvent molecules are omitted for clarity). b) Packing mode projected along the [011] direction, with the interstitial *p*-xylene solvent molecules displayed in pale blue. c) The 2D D_2A layer structure is parallel to the (11–1) plane. In (b) and (c), hydrogen and fluorine atoms have been omitted for clarity.

indicates that the Fermi level of the cathode is shifted to a higher energy by electron-doping via Li^+-ion insertion.

In the LIB system with the **1′**-cathode, the electrons introduced to the cathode during the discharge process should fill the energy states of BTDA-TCNQ because the oxidation state of $[Ru_2]$ is neutral ($[Ru_2^{II,II}]$) (Figure S7, Supporting Information). The reduction of the BTDA-TCNQ moiety following electron-doping via Li^+-ion insertion was confirmed by infrared (IR) spectroscopy. **Figure 4** depicts the IR spectra at room temperature for the pristine sample and the Li^+-ion-inserted cathode (2.66 V vs Li/Li^+), the nominal Li-composition of which was $x = 1$ for $Li_x[\{Ru_2(CF_3CO_2)_4\}_2(\text{BTDA-TCNQ})]\cdot(p\text{-xylene})$ (vide infra). The **1′**-cathode was extracted from the LIB coin cell after Li^+-ion insertion. The stretching vibrational modes of the C≡N groups are clearly observed for both the pristine sample and the Li^+-ion-inserted cathode (2.66 V vs Li/Li^+) at ≈2200 cm^{-1}. However, the peak at ≈2230 cm^{-1} in the neutral pristine sample is shifted to a lower wavenumber (2200 cm^{-1}) in the Li^+-ion inserted cathode. It is known that the reduction of TCNQ*R* shifts this peak to lower wavenumbers,[41,42] e.g., 2232 cm^{-1} for BTDA-TCNQ^0 and 2190 cm^{-1} for $K^+\text{BTDA-TCNQ}^-$.[35] This result proves that the reduction of the BTDA-TCNQ moieties is the dominant occurrence in **1′** following electron-doping through Li^+-ion insertion.

As shown in Figure 1c, one electron-doping into the neutral BTDA-TCNQ moieties is expected to induce ferrimagnetic order through antiferromagnetic exchange interactions between the $S = 1$ spins of the $[Ru_2^{II,II}]$ moieties and the newly generated $S = 1/2$ spin of $\text{BTDA-TCNQ}^{\bullet-}$ (see Figures S8 and S9, Supporting Information). To demonstrate this, magnetization (M) measurements were first carried out ex situ with the **1′**-cathode material extracted from the LIB cell after Li^+-ion insertion. As displayed in **Figure 5**, a hysteresis loop was observed in the magnetic field dependence of M for the Li^+-ion-inserted cathode at 2.66 V versus Li/Li^+. This fact is consistent with the onset of ferrimagnetic order by the generation of a $\text{BTDA-TCNQ}^{\bullet-}$ spin.

The structural variation driven by the accommodation of Li^+-ions was confirmed by synchrotron X-ray diffraction measurements. **Figure 6** shows the powder X-ray diffraction (PXRD) pattern of the material for the Li^+-ion-inserted cathode at 2.66 V versus Li/Li^+. Interestingly, this pattern could be indexed to the monoclinic space group $C2/m$, which is the same as that of the original solvated complex **1**, even though **1′** crystallizes in the triclinic space group P–1. This result indicates that the crystal structure of **1′** is modified during the process of Li^+-ion insertion and, ultimately, the material adopts a structure similar to that of the solvated sample (**1**). Li^+-ions are inserted into the void spaces located in **1′**, accompanied by an expansion of the flexible framework, like recovering to **1**, without a significant collapse of the layered framework. The Li^+-ion-extracted cathode was also checked by the synchrotron PXRD measurement, which confirmed good crystallinity after a discharge/charge cycle (Figure S10, Supporting Information).

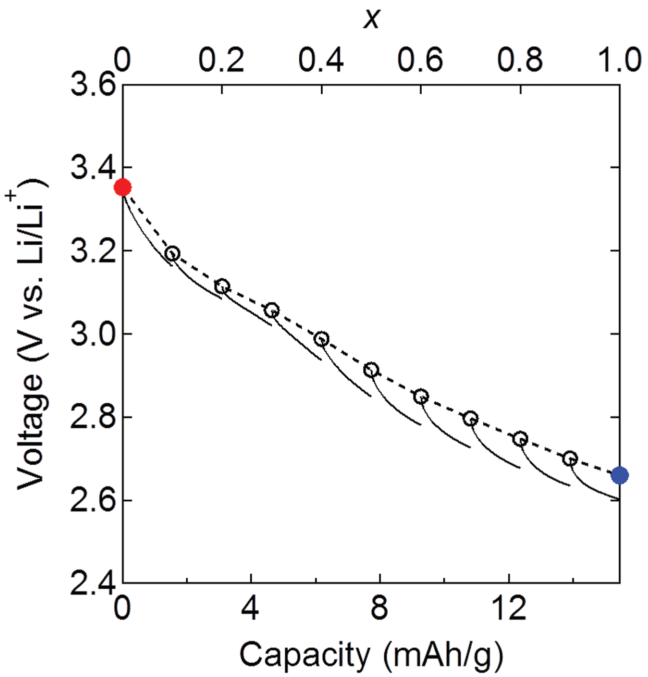

Figure 3. Open circuit voltage as a function of capacity measured in a LIB coin cell combined with the **1′**-cathode (open circles), where the solid line shows the variation in voltage of the LIB cell during the discharge process at a constant current. The red and blue closed circles display the states of the samples taken for ex situ measurements such as the IR, magnetization, and PXRD shown in Figures 4, 5 and 6, respectively (vide infra). The *x* is the nominal Li-composition per formula unit, estimated from the discharged capacity.

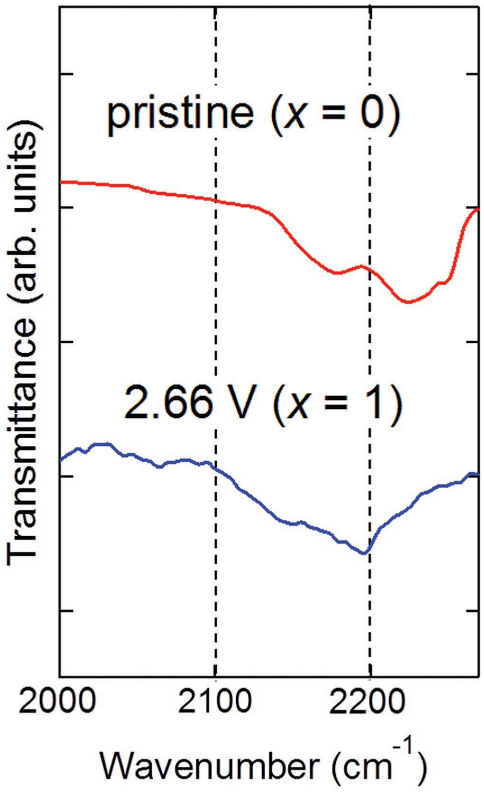

Figure 4. IR spectra of the pristine (**1′**) and the Li$^+$-ion-inserted cathode material (2.66 V vs Li/Li$^+$) measured ex situ as KBr pellets at room temperature.

2.4. In Situ Magnetic Measurements for Band-Filling

For the direct observation of modulated magnetization resulting from electron-doping through Li$^+$-ion insertion, an in situ magnetic measurement system was developed, which consisted of a miniaturized LIB cell suitable for insertion into a commercial superconducting quantum interference device (SQUID); this cell is hereafter called the in situ cell (Figure S11, Supporting Information). The in situ cell was put into a SQUID to elucidate the dependence of the magnetization on the continuous band-filling using an identical sample in LIB cycles. The band-filling was controlled based on the battery voltage to avoid the effect of irreversible capacity.

Figure 7a shows the temperature dependence of the field-cooled magnetization (FCM at $H = 100$ Oe; closed circles) and the remnant magnetization (RM at $H = 0$ Oe; open circles) at several voltages in the in situ cell. The FCM of the pristine cathode (3.26 V vs Li/Li$^+$) and a cathode that had been lightly electron-doped (3.1 V vs Li/Li$^+$) show the typical paramagnetic temperature dependence, consistent with the data obtained in the ex situ measurements. At 3.0 V versus Li/Li$^+$, spontaneous magnetization growth around at 40 K is observed. This result indicates that electron-doping via Li$^+$-ion insertion induces a ferrimagnetic order as the result of electron-filling of the BTDA-TCNQ moieties. As the battery voltage further decreases from 3.0 to 2.9 V, and then to 2.8 V versus Li/Li$^+$,

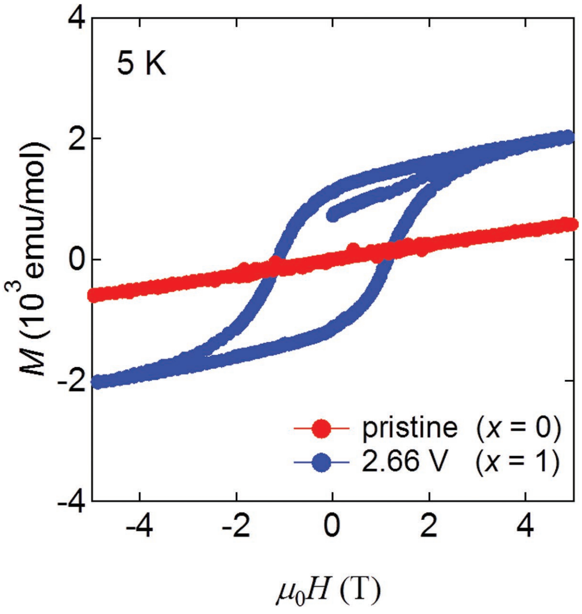

Figure 5. Magnetic field dependence of the magnetization of the cathode material for the pristine (**1′**) and the Li$^+$-ion-inserted material (2.66 V vs Li/Li$^+$) measured ex situ at 5 K.

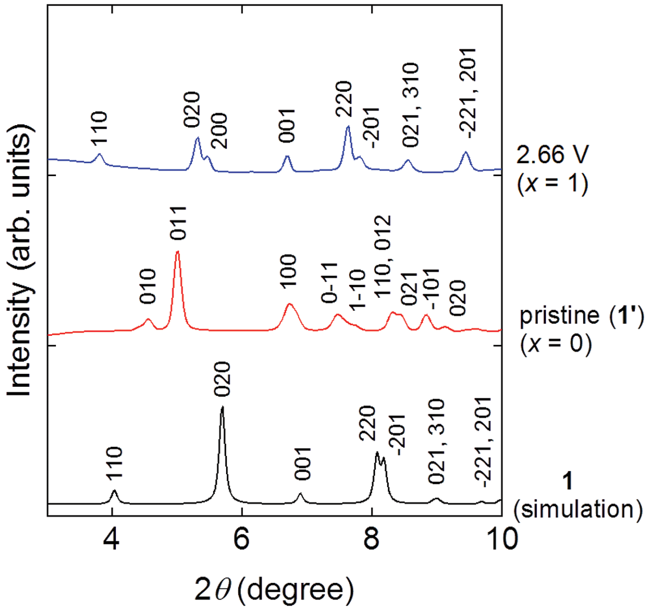

Figure 6. PXRD patterns of the cathode materials for the pristine (**1′**) and the Li$^+$-ion-inserted material (2.66 V vs Li/Li$^+$). A simulated PXRD pattern of the CH_2Cl_2-solvated compound (**1**), estimated from the crystal structure obtained using single-crystal X-ray diffraction analysis, is displayed for comparison (black line).

the Curie temperature (T_C), estimated from the RM disappearance, increases from 40 (3.0 V) to 70 K (2.9 V) and 76 K (2.8 V), accompanied by an obvious increase in the magnetization at 2.9 and 2.8 V compared to that at 3.0 V versus Li/Li$^+$. In the voltage region between 2.8 and 2.65 V versus Li/Li$^+$, the T_C tends to remain constant at around 75 K, but the magnetization is gradually suppressed with the decreasing voltage. Meanwhile, below 2.6 V versus Li/Li$^+$, the T_C suddenly decreases, and when the voltage reaches 2.45 V versus Li/Li$^+$, an increase in the magnetization is no longer observed: the ferrimagnetic order disappears, and the FCM once again exhibits paramagnetic temperature dependence. Thus, spontaneous magnetization generated by doping electrons in the in situ cell only appears in the voltage range 3.0–2.6 V versus Li/Li$^+$.

The observed dependence of magnetization on voltage is clearly attributed to the change of oxidation state in the BTDA-TCNQ moieties. Figure 7b shows the variation in the FCM value at 10 K and the T_C estimated from the RM as a function of voltage, and Figure 7c depicts the variation of $|dQ/dV|$ as a function of the voltage, where $|dQ/dV|$ stands for the differential value (as an absolute value) of capacity (Q) versus voltage (V) as estimated from the OCV curve (Figure S12, Supporting Information). In the $|dQ/dV|$ versus V plot shown in Figure 7c, two peaks are observed at ≈3.1 and 2.6 V versus Li/Li$^+$, indicating that two distinct reduction potentials exist. In **1′**, the [Ru_2] units remain in the neutral [$Ru_2^{II,II}$] state, whereas the

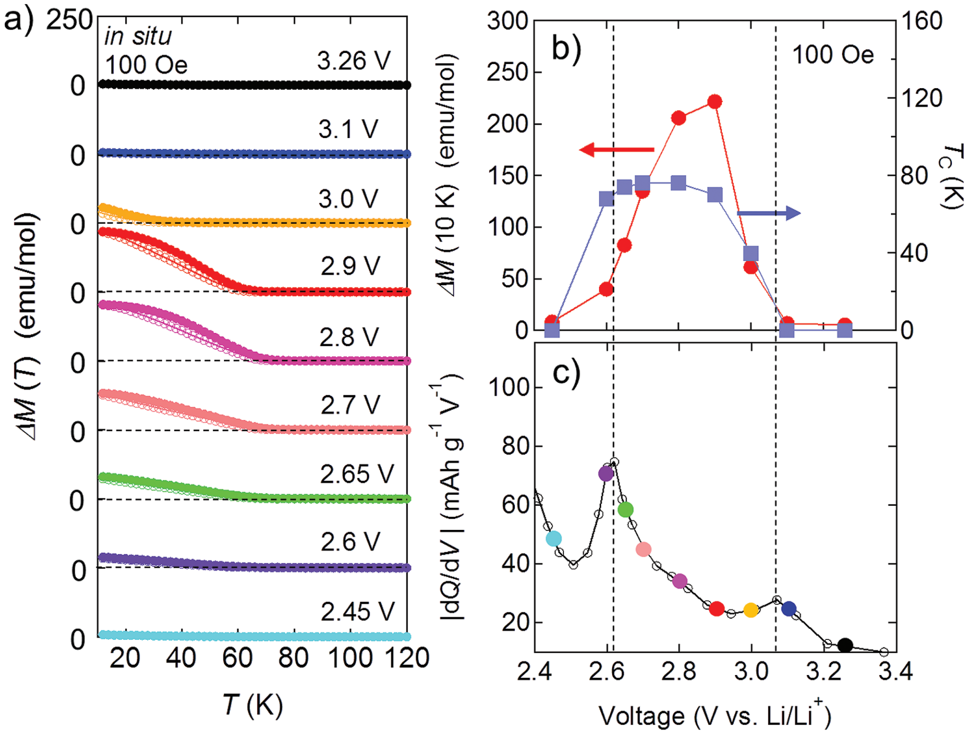

Figure 7. Band-filling dependence of the magnetic states measured using the in situ cell. a) Temperature (T) dependence of the magnetization variation (ΔM) measured using the in situ cell at each battery voltage versus Li/Li$^+$, where $\Delta M(T) \equiv M(T) - M(120\ \text{K})$ and closed and open circles represent FCM and RM, respectively. b) LIB voltage dependence of ΔM at 10 K (closed red circles) and T_C (closed blue squares). The horizontal axis is the cathode voltage associated with the value given in (c). c) The absolute values of the derivative of the capacity (Q) versus the voltage (V), $|dQ/dV|$, which were obtained from the OCV curve measured by GITT (Figure S12, Supporting Information). The voltages given by colored closed circles in (c) correspond to the voltages in (a) at which the magnetization was measured. The vertical dotted lines in (b) and (c) represent the peak positions in the $|dQ/dV|$ plot.

BTDA-TCNQ moiety should experience a sequential two-step reduction from BTDA-TCNQ to BTDA-TCNQ$^{\bullet-}$ and from BTDA-TCNQ$^{\bullet-}$ to BTDA-TCNQ^{2-} (Figure S7, Supporting Information). In the voltage range between these two reduction potentials, the onset of ferrimagnetic order is observed at an identical temperature of about 75 K with a sudden increase in the magnetization, as shown in Figure 7b. Taking into account that $|dQ/dV|$ reflects the density of states of electrons,[49] most of the BTDA-TCNQ/BTDA-TCNQ$^{\bullet-}$ redox couples should become reduced states (1e$^-$-filled states) around the peak corresponding to the first reduction potential, i.e., 3.1 V versus Li/Li$^+$ (Figure S7, Supporting Information). In this situation, the ferrimagnetic order should be constructed through the growth of an exchange-interaction network via BTDA-TCNQ$^{\bullet-}$ (Figure 1c), as observed in Figure 7a,b. On the other hand, in the voltage range below 2.6 V versus Li/Li$^+$, the BTDA-TCNQ$^{\bullet-}$/BTDA-TCNQ^{2-} redox couples should become reduced states (2e$^-$-filled states, Figure S7, Supporting Information). In this case, the ferrimagnetic state should be destabilized relative to the ionic paramagnetic state (2e$^-$-filled state) because A^{2-} ($S = 0$) disconnects the exchange paths (Figure 1c).[35] A similar dependence of the magnetization on the degree of band-filling was also confirmed by ex situ measurements (Figure S13, Supporting Information), proving that the magnetization variation originates from the **1′**-cathode in the inserted LIB cell.

Figure 7b allows the construction of a phase diagram that distinguishes the paramagnetic (PM) and ferrimagnetic (FM) phases of **1′**. Reflecting the oxidation states of BTDA-TCNQ, BTDA-TCNQ^0/BTDA-TCNQ$^{\bullet-}$ and BTDA-TCNQ$^{\bullet-}$/BTDA-TCNQ^{2-}, the T_C displays an almost step-wise change between the PM and FM phases at potentials of ≈3.1 and 2.6 V versus Li/Li$^+$, respectively (an ideal phase diagram should be given in a square; Figure S14, Supporting Information). These results indicate that the Li$^+$-ion insertion into pores and the subsequent migration within the pores involve a smooth electronic reduction in the framework of the LIB system with the **1′**-cathode.

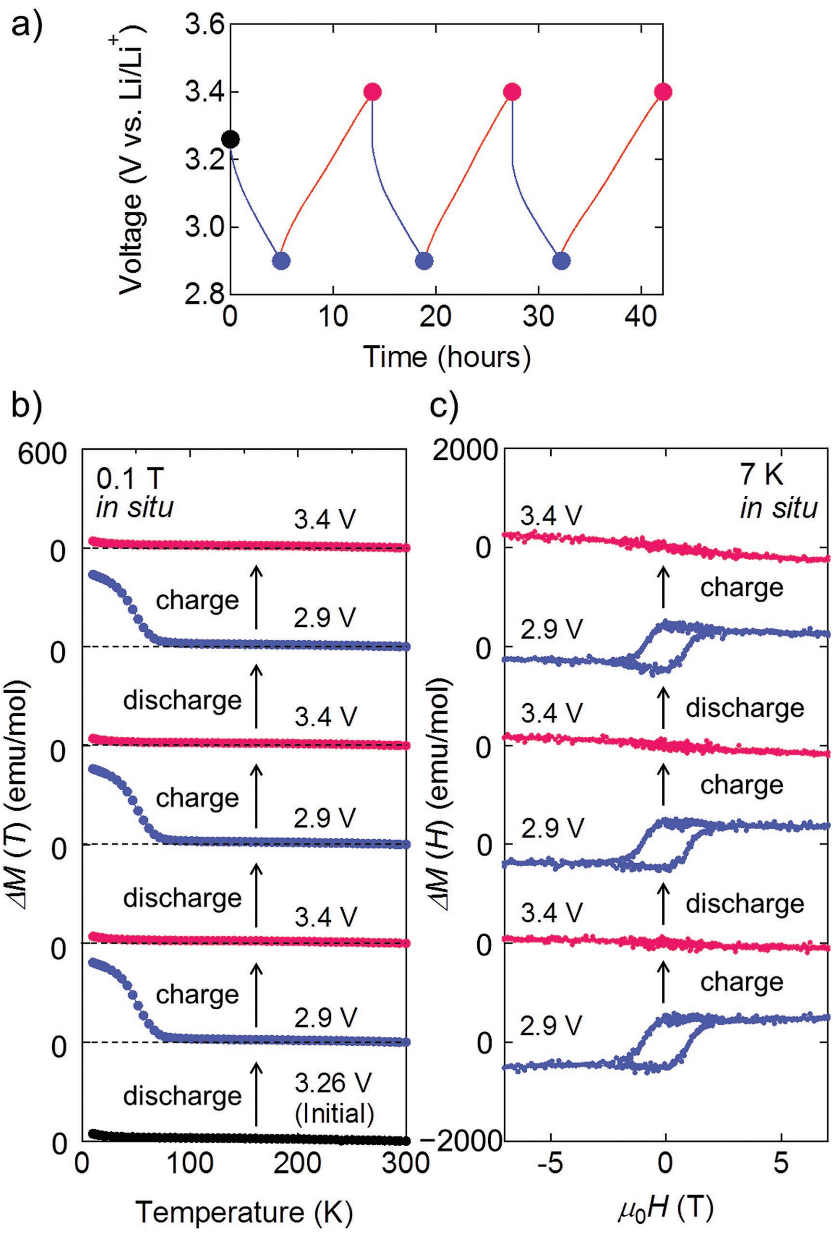

Figure 8. In situ reversible magnetic phase switching. a) The discharge/charge cycles in the in situ cell used for reversible magnetism control (vide infra), where blue and red lines represent the discharge and charge processes, respectively, and the closed circles represent the cathode voltage taken for the in situ magnetization measurements shown in (b) and (c). b) Reversible magnetic phase switching between paramagnetic and ferrimagnetic states, where $\Delta M(T) \equiv M(T) - M$ (300 K). Blue and red curves represent the magnetization of the discharged (Li$^+$-ion-inserted) and charged (Li$^+$-ion-extracted) states, respectively (the initial state is given in black). The curves were measured at the noted voltages corresponding to those represented by closed circles in (a). c) Magnetic field dependence of the magnetization at 7 K for discharged (2.9 V vs Li/Li$^+$) and charged states (3.4 V vs Li/Li$^+$). The magnetization variation from the initial paramagnetic state (M^{initial}), $\Delta M(H) \equiv M(H) - M^{\text{initial}}(H)$, is displayed. Hysteresis curves for the ferrimagnetic phase appear repeatedly in the discharged states.

2.5. Reversible Magnetic Phase Control by In Situ LIB Cycles

Taking advantage of the rechargeability of the LIB system with the **1′**-cathode (Figure S5, Supporting Information), we attempted the reversible control of the magnetic phases using the in situ cell. **Figure 8**a shows the time dependence of voltage for the discharge/charge cycles between 2.9 and 3.4 V versus Li/Li$^+$, and reveals the rechargeability of the LIB with the **1′**-cathode. Following these discharge/charge cycles, the dependence of magnetization on the temperature for each discharged or charged state was measured (Figure 8b). In the respective discharged states (blue curves), the ferrimagnetic order appears repeatedly, with almost the same T_C and the same magnitude of magnetization (Figure 8b). In contrast, the magnetic phase transition completely disappears in all the charged states (red curves). These results indicate that the magnetic phase is reversibly switched between the PM and FM phases through Li^+-ion insertion/extraction in the discharge/charge cycles of the LIB system. As a remarkable answer for the reversible switching of magnetic phases, the open/close cycles of hysteresis phenomenon was demonstrated, in which magnetic field-dependent hysteresis of the magnetization was only observed for the discharge states (Figure 8c).

3. Discussion

Although there are a number of materials where magnetic and electric properties are correlated, it is still a challenge to find a class of materials, which show a reversible giant magneto-electric response. To realize such response, the phase switching in a strongly correlated electron system is one of the effective approaches. Obviously, the discoveries of colossal magnetoresistance in manganites,[50,51] which relates to the phase stability between a charge-orbital order insulator and ferromagnetic metal phases,[52] and the gigantic magneto-electric effect in multiferroic materials,[53,54] which is induced by a phase transition between collinear and spiral spin phases,[55] are representative examples. The magnetic phase switching using an LIB system demonstrated in this work also belongs to the category of giant magneto-electric response realized through an electronic phase transition in a strongly correlated electron system. This magnetic phase switching should be achieved by dynamic band-filling control based on electrochemistry, for which the material should have high porosity and amenability to Li^+-ion migration. That is the reason why we have focused on the family of MOFs composed of donor/acceptor component units (i.e., D/A-MOFs) for use as LIB cathodes.[56–59]

4. Conclusion

In summary, we have succeeded in demonstrating the electrical control of magnetism using a neutral D/A-MOF as the cathode of a LIB system. Reversible magnetic phase switching between the paramagnetic and ferrimagnetic states is closely coupled to the LIB charge/discharge cycles; this is the first demonstration of in situ "magneto-ionic phase switching" in a bulk system by an LIB. The formation of electrochemical equilibrium states is directly associated with the target OCV in an LIB system without further continuous application of an external voltage; hence, the switchable magnetic phases, i.e., **1′**, and the artificial lattices with Li^+–$\mathbf{1'}^-$ and $(Li^+)_2$–$\mathbf{1'}^{2-}$, are nonvolatile after the Li^+-ion insertion/extraction processes. These characteristics might lead to a new type of voltage-programmable nonvolatile memory device. The present technique involving in situ band-filling control based on LIB systems could be expanded to incorporate other redox-active porous molecular systems and may be a key to design long-range magnetic order/electronic correlated states such as superconducting phase. Considering the limited number of MOFs whose intrinsic physical properties are controllable by guest molecules,[60,61] further research probing redox-active paramagnetic MOFs, which can easily accommodate "guest ions", may open up a new avenue of research in the emerging field of magneto-ionics.

5. Experimental Section

Materials Synthesis: All synthetic procedures were performed under anaerobic conditions using Schlenk techniques and ultrapure N_2-filled gloveboxes. Compound **1** was synthesized using a slow diffusion reaction technique: a solution of BTDA-TCNQ (20.0 mg, 0.065 mmol) in CH_2Cl_2 (50 mL) was separated into 2 mL portions and placed in narrow-diameter glass tubes as the bottom layer. A solution of $[Ru_2(CF_3CO_2)_4(THF)_2]$ (100 mg, 0.125 mmol) in *p*-xylene (50 mL) was placed in 2 mL portions over the bottom CH_2Cl_2 layer. The glass tubes were left undisturbed for one week or more to yield black crystals of $[\{Ru_2(CF_3CO_2)_4\}_2(\text{BTDA-TCNQ})]\cdot n CH_2Cl_2\cdot$(*p*-xylene) (**1**). Yield: 36%.

The CH_2Cl_2-free compound, $[\{Ru_2(CF_3CO_2)_4\}_2(\text{BTDA-TCNQ})]\cdot$(*p*-xylene) (**1′**), which was used to investigate magnetism control through an LIB system, was prepared by evacuating a sample of **1** for about 12 h at room temperature. Elemental analysis (%) calculated for **1′**, $C_{36}H_{10}N_8O_{16}F_{24}Ru_4S_2$: C 24.92, H 0.58 N 6.46; found: C 25.311, H 0.527, N 6.953; FT-IR (KBr): ν (C≡N), 2225, 2179 cm^{-1}.

X-Ray Crystallographic Analysis: Crystal data for **1** and **1′** were collected at 112 K on a CCD diffractometer (Saturn 724 VariMax) with graphite monochromated Mo-Kα radiation (λ = 0.71075 Å). Single crystals with dimensions 0.152 × 0.132 × 0.091 and 0.118 × 0.105 × 0.042 mm for **1** and **1′**, respectively, were mounted on thin Kapton films using Nujol and cooled in an N_2 gas stream. The structures were solved using direct methods (SHELX97-2013) and expanded using Fourier techniques. The nonhydrogen atoms were refined anisotropically and the hydrogen atoms were refined using a rigid model. Part of the crystallization solvents in **1** had complicated disorder, which made it difficult to complete the analysis. Thus, after refinement of all the atoms in the framework, the SQUEEZE function was used to determine the contribution of the disordered solvent molecules that could be refined to the structure factors.[62] The contribution of these species was removed from the final structure factor calculations. The void volumes of the crystal structures were determined using PLATON program.[63] Structural diagrams were prepared using the VESTA software.[64]

PXRD experiments for the cathodes were performed with large cylindrical image-plate diffractometers at the High Energy Accelerator Research Organization (KEK), Japan. The incident X-ray beams were monochromatized using Si(111) double crystals. An X-ray beam with a wavelength of λ = 1.003 Å was used for the measurements at BL-8B, the Photon Factory. The wavelength was calibrated on the basis of the polycrystalline CeO_2 diffraction profile. The lattice constant of the Li^+-ion-inserted cathode of **1′** (2.66 V vs Li/Li^+) was estimated using the Le Bail method.[65]

*Crystallographic Data of Compound **1***: $C_{36}H_{10}N_8O_{16}F_{24}Ru_4S_2$, Mr = 1734.88, monoclinic, $C2/m$ (#12), a = 20.323 (4) Å, b = 20.148 (4) Å, c = 8.4363 (14) Å, β = 99.768 (3)°, V = 3404.3(10) Å^3, T = 112 K, Z = 2, D_{calc} = 1.692 g cm^{-3}, F_{000} = 1668.00, λ = 0.71075 Å, μ (Mo Kα) = 10.551 cm^{-1}, 16 260 measured reflections, 5196 unique reflections (R_{int} = 0.0254), R_1 = 0.0391 ($I > 2.00\sigma(I)$), R_1 (all data) = 0.0438, wR_2 = 0.1137 (all data), with GOF (Goodness of fit) = 1.097. CCDC-1497043.

*Crystallographic Data of Compound **1′***.: $C_{36}H_{10}N_8O_{16}F_{24}Ru_4S_2$, Mr = 1734.88, triclinic, P–1 (#2), a = 8.475 (12) Å, b = 13.435 (19) Å, c = 14.10 (2) Å, α = 112.267 (19)°, β = 94.57 (3)°, γ = 95.25 (2)°, V = 1468(4) Å^3, T = 112 K, Z = 1, D_{calc} = 1.963 g cm^{-3}, F_{000} = 834.00, λ = 0.71075 Å, μ (Mo Kα) = 12.237 cm^{-1}, 9543 measured reflections, 5058 unique reflections (R_{int} = 0.0633), R_1 = 0.0907 ($I > 2.00\sigma(I)$), R_1 (all data) = 0.1270, wR_2 = 0.2317 (all data), with GOF = 1.055. CCDC-1497042.

*Crystallographic Data of Li^+-Ion Inserted **1′** at Room Temperature. (2.66 V vs Li/Li^+, x = 1 in $Li_x[\{Ru_2(CF_3CO_2)_4\}_2(BTDA\text{-}TCNQ)\cdot(p\text{-}Xylene)]$)*: Monoclinic, C2/m (#12), a = 21.2963 Å, b = 21.5015 Å, c = 8.685 Å, β = 101.33°, V = 3899.38 Å^3.

Physical Characteristics Measurements: IR spectra were measured as KBr pellets at room temperature using a JASCO FTIR-4200 spectrometer. Thermogravimetric analysis was performed using a Shimadzu DTG-60H instrument under a flowing N_2 atmosphere, and the temperature was increased from room temperature to 400 °C at a rate of 5 °C min^{-1}.

Cathode and Lithium-Ion Battery Cell Preparation: Cathodes were fabricated using a sample of **1′**, acetylene black and polytetrafluoroethylene in a mass ratio of 50:40:10. The mixed active material was pressed on a current collector of aluminum net and dried overnight at room temperature under vacuum. 2032-type coin cells or a miniature LIB cell for in situ magnetization measurements were assembled in an Ar-filled glovebox. The cells consisted of cathodes of **1′**, lithium metal anodes and lithium bis(trifluoromethylsulfonyl) amide (LiTFSA) electrolyte dissolved at 0.30 mol kg^{-1} in *N*-methyl-*N*-propylpyrrolidinium bis(fluorosulfonyl)amide (Py_{13}-FSA).[45]

Ex Situ Magnetic Measurements: Magnetization was measured using a Quantum Design MPMS magnetometer (MPMS-XL-7, MPMS-7S) over the temperature range 1.8–300 K. The magnetic susceptibility of the bulk samples (**1** and **1′**) was corrected for core diamagnetism estimated from the Pascal constants. Li^+-ion insertion into **1′** was performed with a 2032-type coin cell using the GITT[46] with a repeated slow discharge at 1.54 mA g^{-1} for 1 h, followed by a break of 1 h. The OCV was recorded with a potentio-galvanostat (Solartron, 1470E) at 298 K. After Li^+-ion insertion (discharge), the coin cells were disassembled and the cathodes were extracted from the cells in an Ar-filled glovebox. The temperature and magnetic field dependence of the magnetization were measured for the extracted **1′**-cathodes.

In Situ Magnetic Measurements: For the in situ magnetization measurements, a miniature LIB with a quartz cell (15 × 7 × 5 mm; Figure S11, Supporting Information) was prepared. This cell consisted of a Li metal anode, a polypropylene separator, electrolyte (LiTFSA/Py_{13}-FSA) and the cathode including **1′**. A Teflon frame was prepared to set the Li metal anode. Pt plates were used as current collectors for the electrodes. The in situ LIB cell was inserted into a Quantum Design MPMS-7S. Discharging/charging for the in situ LIB cell were conducted to a target voltage under a constant current, 1 mA g^{-1}; each voltage was maintained for 2 h. The discharge/charge control was carried out using a potentio-galvanostat (Solartron, 1287) at 300 K, at which Li^+-ion can migrate in the cathode materials.

[CCDC-1497042 and CCDC-1497043 contain the supplementary crystallographic data for this paper. These data can be obtained free of charge from The Cambridge Crystallographic Data Centre via www.ccdc.cam.ac.uk/data_request/cif.]

Supporting Information

Supporting Information is available from the Wiley Online Library or from the author.

Acknowledgements

The authors thank Dai-ichi Kogyo Seiyaku for supplying the ionic liquid and Dr. M. Nishio (Kanazawa University) for his help with sample preparation. The PXRD measurement was performed under the approval of the Photon Factory Program Advisory Committee (Proposal No. 2014G647). This work was supported by Grants-in-Aid for Scientific Research (nos. 16H02269, 16K05738, 26810029), a Grant-in-Aid for Scientific Research on Innovative Areas ("π-System Figuration" Area 2601, no. 15H00983), a Grant-in-Aid for Challenging Exploratory Research (15K13652) and a MEXT program "Elements Strategy Initiative to Form Core Research Center" (since 2012) from the Ministry of Education, Culture, Sports, Science, and Technology, Japan, the E-IMR project, Support Program for Interdisciplinary Research (FRIS project), the Asahi Glass Foundation, the Hatakeyama Cultural Foundation and the Mitsubishi Foundation.

Received: September 26, 2016
Revised: November 8, 2016

[1] S. Mangin, D. Ravelosona, J. A. Katine, M. J. Carey, B. D. Terris, E. E. Fullerton, *Nat. Mater.* **2006**, *5*, 210.
[2] Y. Shiota, T. Nozaki, F. Bonell, S. Murakami, T. Shinjo, Y. Suzuki, *Nat. Mater.* **2012**, *11*, 39.
[3] M. Saito, K. Ishikawa, S. Konno, K. Taniguchi, T. Arima, *Nat. Mater.* **2009**, *8*, 634.
[4] C. Chappert, A. Fert, F. N. V. Dau, *Nat. Mater.* **2007**, *6*, 813.
[5] F. Matsukura, Y. Tokura, H. Ohno, *Nat. Nanotechnol.* **2015**, *10*, 209.
[6] M. Fiebig, *J. Phys. D* **2005**, *38*, R123.
[7] H. Ohno, D. Chiba, F. Matsukura, T. Omiya, E. Abe, T. Dietl, Y. Ohno, K. Ohtani, *Nature* **2000**, *408*, 944.
[8] D. Chiba, M. Sawicki, Y. Nishitani, Y. Nakatani, F. Matsukura, H. Ohno, *Nature* **2008**, *455*, 515.
[9] Y. Yamada, K. Ueno, T. Fukumura, H. T. Yuan, H. Shimotani, Y. Iwasa, L. Gu, S. Tsukimoto, Y. Ikuhara, M. Kawasaki, *Science* **2011**, *332*, 1065.
[10] M. Weisheit, S. Fähler, A. Marty, Y. Souche, C. Poinsignon, D. Givord, *Science* **2007**, *315*, 349.
[11] T. Maruyama, Y. Shiota, T. Nozaki, K. Ohta, N. Toda, M. Mizuguchi, A. A. Tulapurkar, T. Shinjo, M. Shiraishi, S. Mizukami, Y. Ando, Y. Suzuki, *Nat. Nanotechnol.* **2009**, *4*, 158.
[12] D. Chiba, S. Fukami, K. Shimamura, N. Ishikawa, K. Kobayashi, T. Ono, *Nat. Mater.* **2011**, *10*, 853.
[13] S. Shimizu, K. S. Takahashi, T. Hatano, M. Kawasaki, Y. Tokura, Y. Iwasa, *Phys. Rev. Lett.* **2013**, *111*, 216803.
[14] U. Bauer, S. Emori, G. S. D. Beach, *Nat. Nanotechnol.* **2013**, *8*, 411.
[15] S. Emori, U. Bauer, S. Woo, G. S. D. Beach, *Appl. Phys. Lett.* **2014**, *105*, 222401.
[16] U. Bauer, L. Yao, A. J. Tan, P. Agrawal, S. Emori, H. L. Tuller, S. Dijken, G. S. D. Beach, *Nat. Mater.* **2015**, *14*, 174.
[17] Y. N. Yan, X. J. Zhou, F. Li, B. Cui, Y. Y. Wang, Y. G. Wang, F. Pan, C. Song, *Appl. Phys. Lett.* **2015**, *107*, 122407.
[18] X. Zhou, Y. Yan, J. Miao, B. Cui, F. Pan, C. Song, *J. Phys. Chem. C* **2016**, *120*, 1633.
[19] K. Duschek, D. Pohl, S. Fähler, K. Nielsch, K. Leistner, *APL Mater.* **2016**, *4*, 032301.
[20] D. A. Gilbert, J. Olamit, R. K. Dumas, B. J. Kirby, A. J. Grutter, B. B. Maranville, E. Arenholz, J. A. Borchers, K. Liu, *Nat. Commun.* **2016**, *7*, 11050.
[21] K. Leistner, J. Wunderwald, N. Lange, S. Oswald, M. Richter, L. Schultz, S. Fähler, *Phys. Rev. B* **2013**, *87*, 224411.
[22] T. Tsuchiya, K. Terabe, M. Ochi, T. Higuchi, M. Osada, Y. Yamashita, S. Ueda, M. Aono, *ACS Nano* **2016**, *10*, 1655.
[23] V. Silvakumar, C. A. Ross, N. Yabuuchi, Y. Shao-Horn, K. Persson, G. Ceder, *J. Electrochem. Soc.* **2008**, *155*, 83.
[24] S. Dasgupta, B. Das, M. Knapp, R. A. Brand, H. Ehrenberg, R. Kruk, H. Hahn, *Adv. Mater.* **2014**, *26*, 4639.
[25] T. Yamada, K. Morita, K. Kume, H. Yoshikawa, K. Awaga, *J. Mater. Chem. C* **2014**, *2*, 5183.
[26] G. Gershinsky, E. Bar, L. Monconduit, D. Zitoun, *Energy Environ. Sci.* **2014**, *7*, 2012.
[27] M. Okubo, K. Kagesawa, Y. Mizuno, D. Asakura, E. Hosono, T. Kudo, H. Zhou, K. Fujii, H. Uekusa, S. Nishimura, A. Yamada, A. Okazawa, N. Kojima, *Inorg. Chem.* **2013**, *52*, 3772.

[28] O. Sato, T. Iyoda, A. Fujishima, K. Hashimoto, *Science* **1996**, *271*, 49.
[29] O. Sato, S. Hayami, Y. Einaga, Z. Z. Gu, *Bull. Chem. Soc. Jpn.* **2003**, *76*, 443.
[30] O. Sato, *J. Solid State Electrochem.* **2007**, *11*, 773.
[31] M. Okubo, D. Asakura, Y. Mizuno, T. Kudo, H. Zhou, A. Okazawa, N. Kojima, K. Ikedo, T. Mizokawa, I. Honma, *Angew. Chem., Int. Ed.* **2011**, *50*, 6269.
[32] Y. Mizuno, M. Okubo, K. Kagesawa, D. Asakura, T. Kudo, H. Zhou, K. Oh-ishi, A. Okazawa, N. Kojima, *Inorg. Chem.* **2012**, *51*, 10311.
[33] T. Yamada, K. Morita, H. Wang, K. Kume, H. Yoshikawa, K. Awaga, *Angew. Chem., Int. Ed.* **2013**, *52*, 6238.
[34] C. H. Li, M. K. Perah, D. Asakura, M. W. Meisel, M. Okubo, D. R. Talham, *Chem. Mater.* **2015**, *27*, 1524.
[35] K. Taniguchi, K. Narushima, J. Mahin, W. Kosaka, H. Miyasaka, *Angew. Chem., Int. Ed.* **2016**, *55*, 5238.
[36] V. Etacheri, R. Marom, R. Elazari, G. Salitra, D. Aurbach, *Energy Environ. Sci.* **2011**, *4*, 3243.
[37] H. Miyasaka, *Acc. Chem. Res.* **2013**, *46*, 248.
[38] N. Motokawa, S. Matsunaga, S. Takaishi, H. Miyasaka, M. Yamashita, K. R. Dunber, *J. Am. Chem. Soc.* **2010**, *132*, 11943.
[39] H. Fukunaga, H. Miyasaka, *Angew. Chem., Int. Ed.* **2015**, *54*, 569.
[40] K. Nakabayashi, M. Nishio, K. Kubo, W. Kosaka, H. Miyasaka, *Dalton Trans.* **2012**, *41*, 6072.
[41] W. Kosaka, T. Morita, T. Yokoyama, J. Zhang, H. Miyasaka, *Inorg. Chem.* **2015**, *54*, 1518.
[42] H. Miyasaka, N. Motokawa, S. Matsunaga, M. Yamashita, S. Sugimoto, T. Mori, N. Toyota, K. R. Dunber, *J. Am. Chem. Soc.* **2010**, *132*, 1532.
[43] F. A. Cotton, R. A. Walton, *Multiple Bonds Between Metal Atoms*, 2nd ed., Oxford University Press, Oxford **1993**.
[44] M. Nishio, H. Miyasaka, *Inorg. Chem.* **2014**, *54*, 4716.
[45] H. Matsumoto, H. Sakaebe, K. Tatsumi, M. Kikuta, E. Ishiko, M. Kono, *J. Power Sources* **2006**, *160*, 1308.
[46] W. Weppner, R. A. Huggins, *J. Electrochem. Soc.* **1977**, *124*, 1569.
[47] J. B. Goodenough, K.-S. Park, *J. Am. Chem. Soc.* **2013**, *135*, 1167.
[48] A. J. Bard, L. R. Faulkner, *Electrochemical Methods: Fundamentals and Applications*, 2nd ed., John Wiley & Sons, New York **2001**.
[49] J. R. Dahn, J. N. Reimers, T. Tiedje, Y. Gao, A. K. Sleigh, W. R. McKinnon, S. Cramm, *Phys. Rev. Lett.* **1992**, *68*, 835.
[50] S. Jin, T. H. Tiefel, M. McCormack, R. A. Fastnacht, R. Ramesh, L. H. Chen, *Science* **1994**, *264*, 413.
[51] Y. Tokura, A. Urushibara, Y. Moritomo, T. Arima, A. Asamitsu, G. Kido, N. Furukawa, *J. Phys. Soc. Jpn.* **1994**, *63*, 3931.
[52] Y. Tokura, *Rep. Prog. Phys.* **2006**, *69*, 797.
[53] T. Kimura, T. Goto, H. Shintani, K. Ishizaka, T. Arima, Y. Tokura, *Nature* **2003**, *426*, 55.
[54] K. Taniguchi, N. Abe, T. Takenobu, Y. Iwasa, T. Arima, *Phys. Rev. Lett.* **2006**, *97*, 097203.
[55] T. Arima, *J. Phys. Soc. Jpn.* **2011**, *80*, 052001.
[56] G. Férey, F. Millange, M. Morcrette, C. Serre, M.-L. Doublet, J.-M. Grenèche, J.-M. Tarascon, *Angew. Chem., Int. Ed.* **2007**, *46*, 3259.
[57] A. Fateeva, P. Horcajada, T. Devic, C. Serre, J. Marrot, J.-M. Grenèche, M. Morcrette, J.-M. Tarascon, G. Maurin, G. Férey, *Eur. J. Inorg. Chem.* **2010**, *2010*, 3789.
[58] Z. Zhang, H. Yoshikawa, K. Awaga, *J. Am. Chem. Soc.* **2014**, *136*, 16112.
[59] Z. Zhang, H. Yoshikawa, K. Awaga, *Chem. Mater.* **2016**, *28*, 1298.
[60] S. S. Kaye, H. J. Choi, J. R. Long, *J. Am. Chem. Soc.* **2008**, *130*, 16921.
[61] M.-H. Zeng, Z. Yin, Y.-X. Tan, W.-X. Zhang, Y.-P. He, M. Kurmoo, *J. Am. Chem. Soc.* **2014**, *136*, 4680.
[62] A. L. Spek, *J. Appl. Cryst.* **2003**, *36*, 7.
[63] A. L. Spek, *Acta Crystallogr. Sect. A* **1990**, *46*, 194.
[64] K. Momma, F. Izumi, *J. Appl. Cryst.* **2008**, *41*, 653.
[65] A. L. Bail, H. Duroy, J. L. Fourquet, *Mater. Res. Bull.* **1988**, *23*, 447.